Mechanical Systems and Signal Processing 196 (2023) 110335

Contents lists available at ScienceDirect

Mechanical Systems and Signal Processing

journal homepage: www.elsevier.com/locate/ymssp

Evaluation of root stresses of a rattling gear pair

A. Donmez *, C. Thomas, A. Kahraman, M. Handschuh

Department of Mechanical and Aerospace Engineering, The Ohio State University, Columbus, OH 43210, USA

ARTICLE INFO

Keywords:
Gear rattle
Root stress
Rattle experiments
Vibro-impacts

ABSTRACT

Gear rattle is a major noise problem in certain powertrains systems, especially those that are driven by internal combustion engines such as timing gear drives, engine balancers or manual transmissions. Teeth lose contact intermittently to commit impacts along the drive and coast sides of the gear pairs having backlash. Most of the studies on this topic focused exclusively on the noise and vibration consequences of rattle with a very little attention given to its influence on system durability. This study presents an experimental investigation of tooth root stresses of a spur gear pair during periodic and chaotic rattling motions caused by a harmonically time-varying input torque. Root stresses of certain teeth of one of the gears are measured in the instances when these teeth are in gear mesh zone when impacts occur. Changes to root stress time histories due to drive and coast-side impacts are documented to show that root stress amplitudes are increased significantly by impacts. Measurements also indicate that most impacts generate families of fully-released strain peaks that contribute the fatigue damage along the drive and coast sides root fillets. A deformable-body model was shown to simulate the experiments accurately, so that it can be used to predict statistical distributions for root stress duty cycles for estimation of fatigue lives of rattling gears.

1. Introduction

A lightly loaded gear pair that is subjected to input and/or output torque fluctuations often exhibits a vibro-impact behavior, called *rattling*, and in some more severe cases, *hammering*. Gear rattle has been observed in various powertrain systems of ground vehicles from manual transmission and engine balancer to diesel engine timing gear sets. In those applications, torque fluctuations are primarily caused by firing pulses of the internal combustion engine (ICE). In manual transmissions, these ICE torque fluctuations result in impacts of unloaded gear pairs with small contact forces [1] such that manual transmission rattle problems have mostly been treated as a noise problem [2–8] with little durability concerns. Diesel engine timing gear trains, on the other hand, are subjected to additional torque fluctuations on the output side due to cam drive and other auxiliary units such as fuel pump, air compressor and lube pump. In such cases, contact forces at the impact events can be large causing amplified root stresses arising durability concerns [9]. With recent trends towards increasing injection pressures to lower fuel consumption and vehicle emissions, today's powertrains are subjected to even higher torque fluctuations and increased rattle risk [10].

Most of the rattle studies in timing gear applications focused on gear rattle problems of specific engines or engine prototypes so that input and output fluctuations were produced by an actual ICE [10–13]. These studies employed engine noise measurements to investigate the noise reduction performance of design features such as reducing the backlash of a single gear pair [14], and crank and

* Corresponding author.
E-mail address: Donmez.4@osu.edu (A. Donmez).

https://doi.org/10.1016/j.ymssp.2023.110335
Received 11 November 2022; Received in revised form 9 February 2023; Accepted 29 March 2023

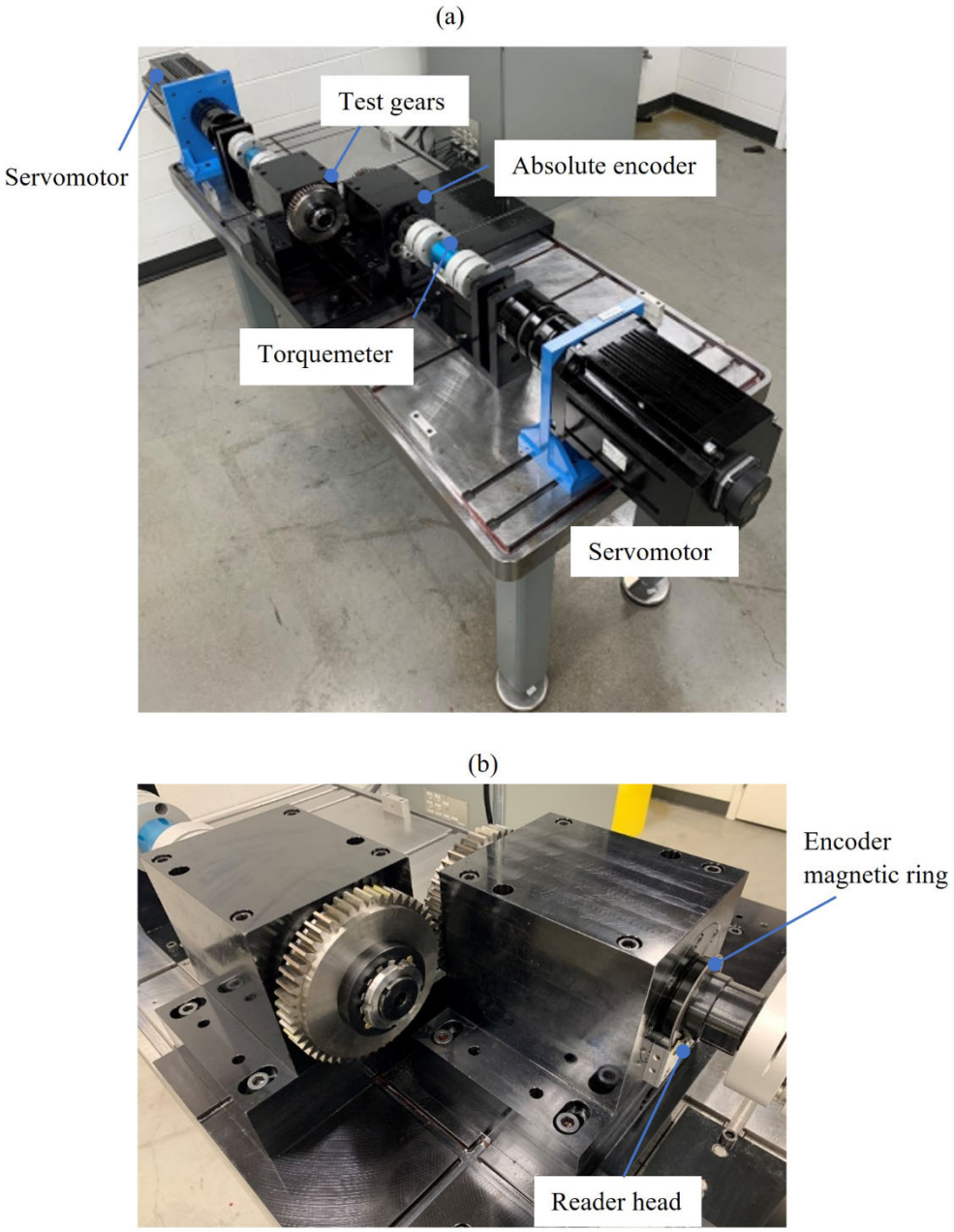

Fig. 1. (a) The rattle test set-up and (b) a close-up view showing one of the absolute encoders.

camshaft torsional vibration isolators [11]. In spite of all these experimental studies concerning the noise outcome of gear rattle, attempts to quantify the root stresses under rattling conditions have been rather sparse. The study by Pfeiffer and Prestl [9] appears to be one of the first studies on the effect of large impact forces on life span of the gears. In this study, a dynamic model of the timing gear train subjected to crankshaft torsional vibrations as well as output fluctuations due to cam mechanism, fuel pump, and other auxiliary units was proposed to predict the motion from which gear mesh forces can be calculated. Validation of that model was conducted through comparison of measured and predicted vibration data without any direct root strain measurements. More recently, Ziegler and Eberhard [15] proposed an experimental methodology to validate their deformable-body model that investigates the root stress under impacts. In their experimental set-up, a sphere was employed as an impact body while the investigated gear was fixed to the test bed.

In a set of recent studies, authors presented experimental and theoretical studies of rattling of single and multi-mesh gear trains with primary focus on characterization of the nonlinear behavior [16,17] and relating the torsional dynamic behavior to the resultant noise levels [18,19]. A pair of companion studies extended this framework by investigating the influence of backlash amplitudes [20] and gear manufacturing errors [21] on rattle, again with a noise and vibration emphasis.

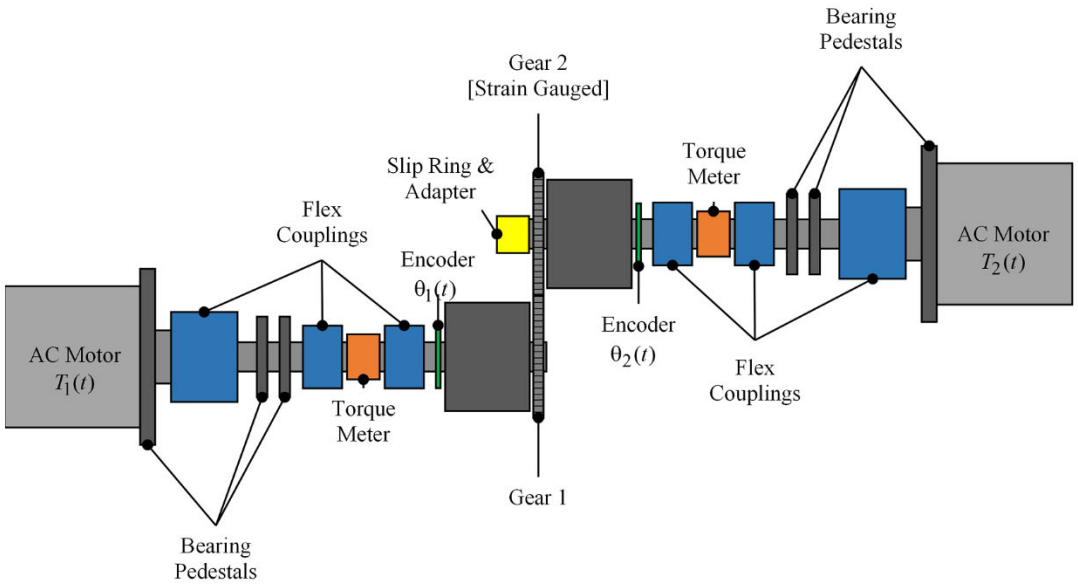

Fig. 2. A top view schematic of the rattle test machine set-up.

Apparent lack of interest in investigation of root stress under rattling stems from unloaded operating conditions of the manual transmission rattle problem subjected to input fluctuations only. Under severe cyclic torque demand of timing gear set rattling applications, gear rattle can result in root stresses that impact fatigue damage and the resultant reliability of the gear train. Currently, there is very limited experimental data regarding the durability consequences of gear rattle. Furthermore, existing gear pair models that can predict root stresses under rattling conditions lack validation. As such, the overall goal of this study is to devise an experimental methodology to investigate root stress consequences of rattling motions of a gear pair. Specific objectives of this study are as follows: (i) develop an experimental methodology that is capable of measuring tooth root stresses of rattling gear pairs; (ii) device a deformable-body dynamic model of the experimental set-up to predict dynamic root stresses during rattling motions; (iii) correlate the model predictions and measurements to assess the accuracy of the model; and (iv) determine operating parameters and types of rattling motions that are more prominent in terms of resultant root stress conditions.

On the modeling side, great majority of the published gear rattle models [1,2,4–8] were discrete models where the gear mesh interface was represented by discrete spring and damper elements subject to backlash. Such discrete models cannot predict stresses measured in this study. As such, a deformable-body dynamic model of a gear pair that can include tooth separations under rattling conditions will be employed in this study.

2. Experimental methodology

2.1. Test set-up

An existing gear rattle test set-up to simulate typical real-life torque fluctuations in a laboratory environment [18,19] will be employed. Fig. 1(a) shows this test set-up. Only the details that are relevant to this study will be provided here while all other details of the test machine can be found in Ref. [18]. Here, two identical spindles were driven by 11 kW three-phase synchronous AC motors to generate torque and/or speed fluctuations at desired shapes, amplitudes and frequencies. A top view schematic of the test machine of Fig. 1 is shown in Fig. 2 to highlight its main components. Measurement of the torsional vibrations of both spindles along with the backlash boundaries at the drive and coast sides is of critical importance here in order to characterize the rattling behavior and mark the instances of drive and coast-side impacts. The test set-up measures rotational motion of each gear i, $\theta_i(t)$, $i = 1,2$, simultaneously through absolute encoders placed on flanges of each gear. The close-up image of Fig. 1(b) shows one of the absolute encoders. Each encoder had 20 bits of resolution and consisted of a read-head, suitable for the RS422 signaling standard, and a magnetic ring. The data analysis system allowed the measurements from both encoders, $\theta_1(t)$ and $\theta_2(t)$, to be synchronous. The relative gear mesh displacement $q(t)$ is the focus here rather than the individual rotational displacements of each gear. It is defined along the line of action as

$$q(t) = r_1\theta_1(t) - r_2\theta_2(t). \tag{1}$$

Based on the operating test conditions, rattling gear pairs can display various motions by spanning different contact regimes. Fig. 3 (a) demonstrates these contact regimes [16]. Here, any motion characterized by the continuous contact along the drive side of the gear pair is called a no-impact (NI) motion. In this case, the motion is contained within Regime I. In case when instantaneous tooth separations from drive side take place without any coast-side contact, Regime II of Fig. 3(a) along with Regime I defines the motion that is conventionally called a single-sided-impact (SSI) motion. Lastly, a motion involving Regime III in addition to the other two regimes,

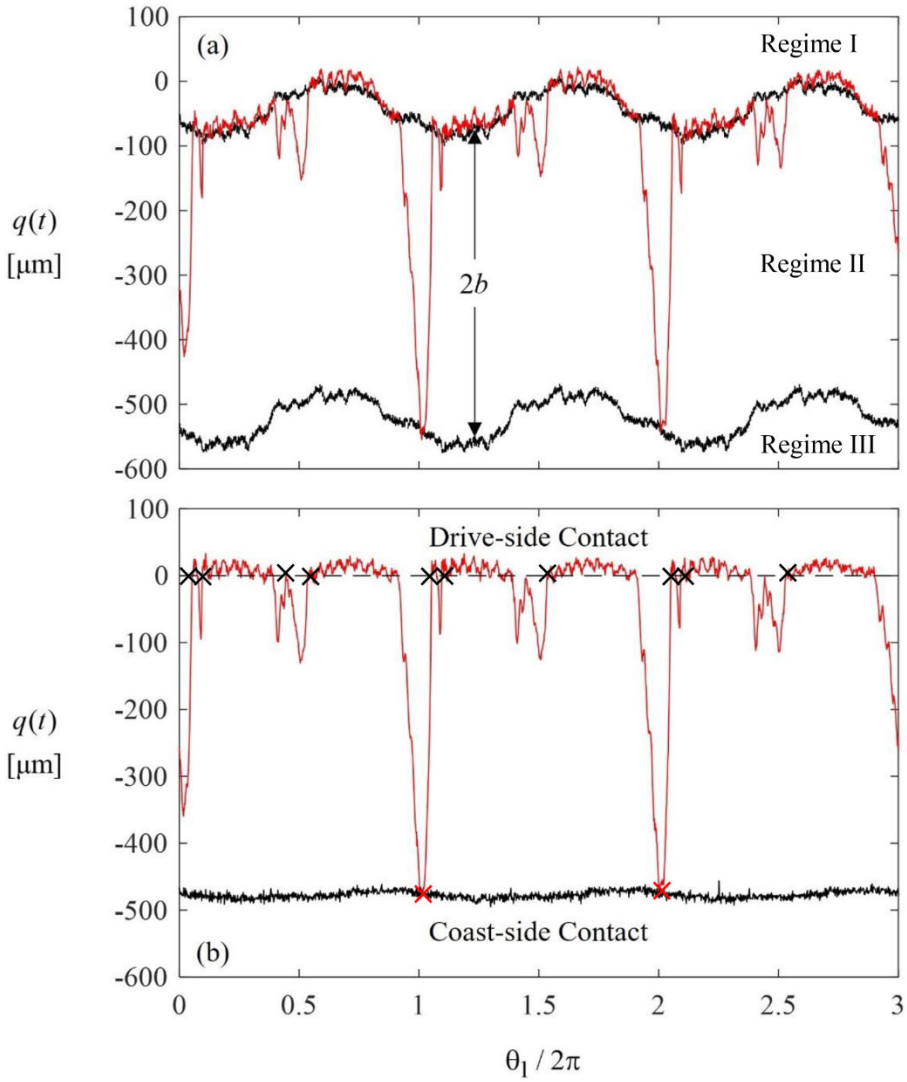

Fig. 3. An example $q(t)$ signal with (a) drive and coast-side backlash boundaries and (b) the drive-side boundary signal used as reference. Black lines denote backlash boundaries and marker 'x' denote impact events.

both drive and coast-side contacts are possible, separated by periods of no contact at all. This type of motions is called here double-sided impact (DSI) motions.

Considering that the impacts take place at the boundaries of these three regimes, specifically at instances of transition from Regime II to Regime I and from Regime II to Regime III, $q(t)$ must be viewed together with the drive and coast-side backlash boundaries. The backlash boundaries were established as a function of rotational angles by employing the method proposed in Ref. [18]. The drive-side boundary was obtained by applying a small mean torque (say 1 Nm) while setting alternating torque amplitude to zero to maintain tooth contact along the drive-side at a low input speed of 50 rpm. The same process was repeated next with small negative mean torque applied to the gear pair such that the contact is on the coast side continuously to establish the back-side backlash boundary. Fig. 3(a) shows an example measured $q(t)$ (red line) generated from measured synchronous $\theta_1(t)$ and $\theta_2(t)$ using Eq. (1). In the same figure, measured drive and coast-side backlash boundaries (black lines) are also displayed. With this, when $q(t)$ is above the drive-side backlash boundary, there is contact along the drive side and the motion is in Regime I of Fig. 3(a). Likewise, at the instances when $q(t)$ is below the coast-side backlash boundary, there is contact along the coast side with the motion being in Regime III of Fig. 3(a). The area between the two backlash boundaries is Regime II when there is no contact between gear teeth. The distance between the boundaries represents the backlash magnitude $2b$ along the line of action of the gears. While manufacturing errors such as gear eccentricities and tooth spacing errors might introduce a rotation-depended variations $2b$ is nearly constant in Fig. 3(a) since the gears are of high accuracy. In Fig. 3(b), the drive-side boundary signal was used as reference and subtracted from $q(t)$ as well as both backlash boundaries. In this case, the drive side backlash boundary becomes $q(t)= 0$ line and the crossings of $q(t)$ through this boundary in the upward direction represent drive-side impacts. Also seen in this figure that, the back-side boundary is not flat with

Table 1
Basic design parameters for spur gears used in this study. All units are in mm unless specified.

Parameter	Values	
	Gear 1	Gear 2
Number of Teeth	50	
Normal Module	3.00	
Pressure Angle (deg)	20.00	
Pitch Diameter	150.00	
Base Diameter	140.954	
Major Diameter	155.42	154.68
Minor Diameter	140.68	
Circular Tooth Thickness	4.64	
Active Face Width	20.00	

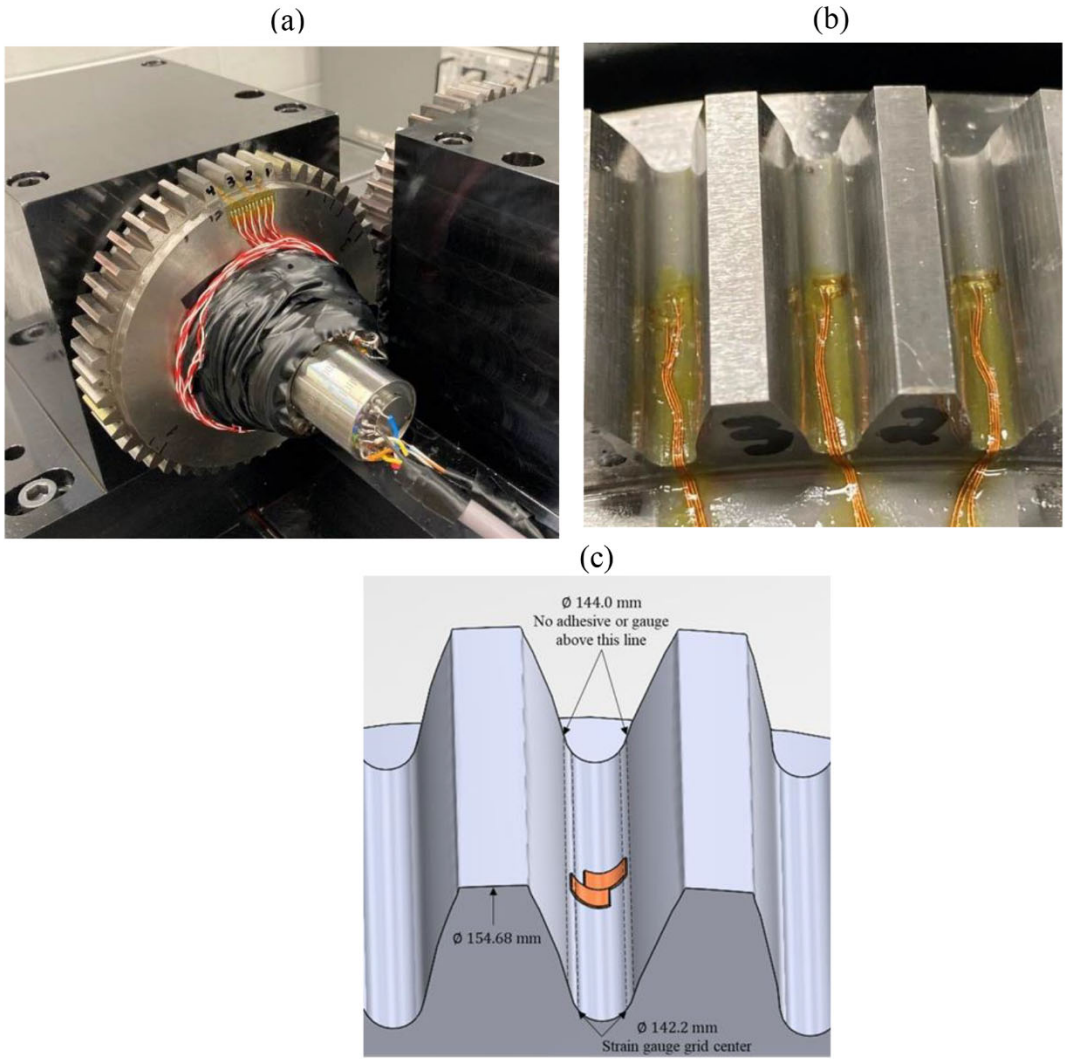

Fig. 4. An image of (a) the instrumented test gear pair on the test machine, (b) a close-up images of the strain gauged tooth roots, and (c) a schematic defining gauge locations.

some minor variations due to unavoidable manufacturing errors. The backlash magnitude in this case is $2b = 478 \pm 16$ μm, which can be considered constant for practical purposes.

Two independently controlled, three-phase synchronous AC motors shown in Fig. 1(a) and Fig. 2 generate input and output torque fluctuations on opposite ends of the test machine. The motors can achieve a rotational speed of 3000 rpm and user-defined torque

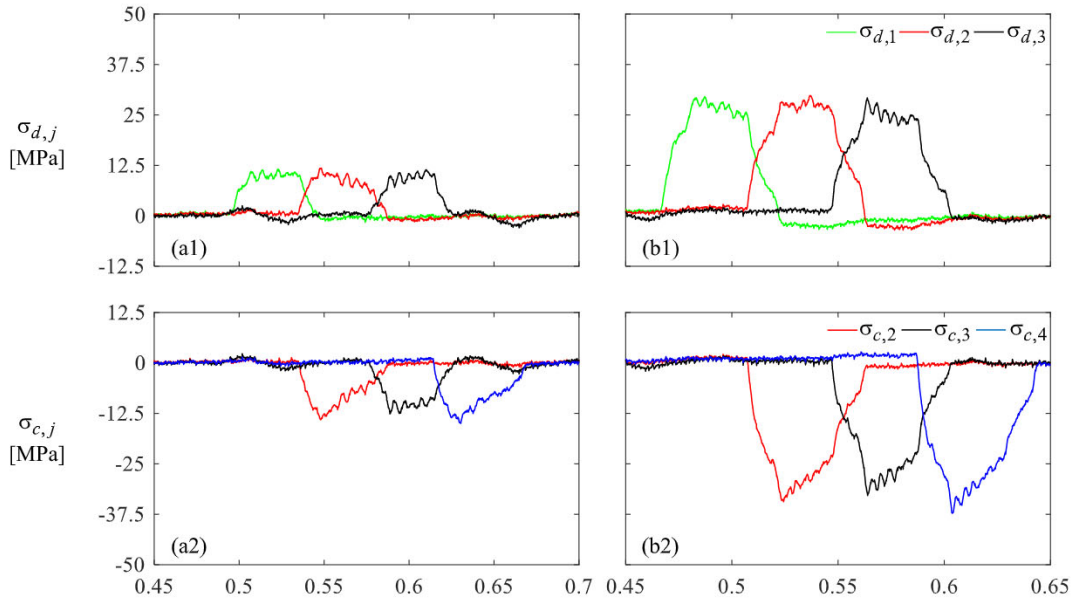

Fig. 5. Measured stress time histories at $T_{a1} = T_{a2} = 0$, (a) $T_m = 10$ Nm and (b) $T_m = 30$ Nm. (a1,b1) are the drive-side stresses, and (a2,b2) are the coast side stresses.

profiles ($i = 1, 2$)

$$T_i(t) = T_{mi} + T_{ai}(t) \tag{2}$$

The mean torque amplitudes are related such that $T_m = T_{m1} = (r_2/r_1)T_{m2}$ where r_i is the base radius of gear i. Only input torque fluctuations will be considered in this study such that $T_{a2}(t) = 0$. The input alternating torque $T_{a1}(t)$ is defined as a function of input rotational motion θ_1(t) such that

$$T_{a1}(t) = T_{a1}\ \sin[n_1\theta_1(t)\ +\ n_1\phi] \tag{3}$$

where T_{a1} is the input torque fluctuation amplitude. The rotational motion of axis-i can be represented by a sum of a kinematic trajectory $\Omega_i t$ and alternating part $\overline{\theta}_i(t)$ (i.e.,$\theta_i(t) = \overline{\theta}_i(t) + \Omega_i t$ where Ω_i is the set nominal speed). Then, the period τ of induced torque fluctuation $T_{a1}(t)$ can be determined by neglecting the small frequency modulations caused by $\overline{\theta}_1(t)$ such that $\tau = 2\pi/(n_1\Omega_1)$. With this, the input torque fluctuation has a frequency that is n_1 times the rotational frequency. While the test machine allows user to set any n_1 value, it is typical that n_1 is an integer (say $n_1 = 2$ or 3 based on the number of cylinders of the ICE). Phase angle parameter ϕ in Eq. (3) represents the relation between the torque fluctuation and angle of a reference tooth on gear 1. If this reference tooth is instrumented with a strain gauge, then depending on the value of ϕ, this tooth can be brought into the gear mesh zone at any instant in relation to the measured $q(t)$, particularly at the instances of impacts.

2.2. Test specimens and root strain measurement

The unity-ratio gear pair used in this study was from a family of spur gears used in several earlier dynamics [22–24] and quasi-static [25,26] studies. Table 1 lists its basic design parameters. Teeth were unmodified in the profile direction (pure involute shapes) while having 4 μm lead crown each. Given the high accuracy of test gears with unmodified profiles, manufacturing error related effects can be deemed to be negligible. For the experiments, the operating center distance was set to 150.5 mm, resulting in a backlash magnitude of $2b = 470$ μm along the line of action.

Experiments were performed under mist lubrication. As such, effects of lubrication on the resultant rattle conditions were assumed to be negligible. This assumption might not hold for the cases when gears are subjected to more oil (e.g., dip lubrications) at the contact interfaces. Such experiments have been left to future work along with adding hydrodynamic damping mechanisms to accompanying model as in Ref. [7].

While tedious, placing strain gauges to roots of a gear to record dynamic tooth bending stresses is not new. There are many successful examples of it in the literature (e.g. Refs. [27–30]). Almost all of these studies considered accurate gears operating under constant torque values such that instrumenting any teeth of the gear would produce essentially the same stress profile. This study uses the same strain gauging method with the experimental set-up from our earlier rattle studies to measure stresses of a rattling gear. There are three essential components for this to be effective: (1) accurate and deliberate gauging of a gear, (2) having a test set-up that can impose precise torque profiles to cause certain specified rattle motions that are measured, and (3) a method of adjusting the phase angle between the torque fluctuations and the gauged tooth of the gear such that the tooth experiences various impacts properly. This

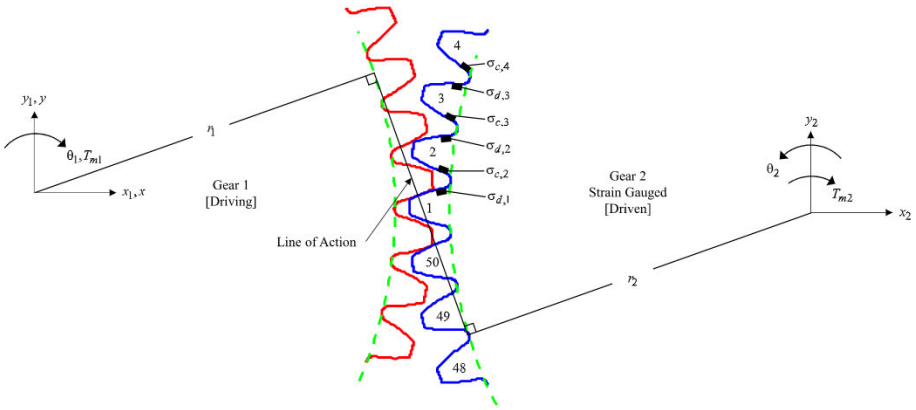

Fig. 6. A schematic showing the strain gauge tooth positions, clocking, and phasing methodology.

makes the task in hand significantly more challenging than those earlier constant-torque measurements.

Gear 2 in Table 1 was instrumented with six miniature strain gauges (Vishay Micro-Measurements EA-06-015LA-120) on three consecutive root fillets. Fig. 4(a) shows the gauged gear mounted on the test machine, and Fig. 4(b) is a close-up view of the three gauged root fillets while Fig. 4(c) defines the locations of a pair of gauges in a root fillet. Here both gauges are centered along the face width so that they are as close to the mid-plane of the teeth as possible (at a 0.38 mm offset). Higher edges of both gauges were forced to stay below the 72 mm radius (comfortably below the nominal start of the active profile) so that the gauges are protected. One of the gauges of each root spanned the drive side of while the other one mirrored the first one on the coast side. Each gauge had a gauge factor of 2.09 and a resistance of 120 Ohm. They were open-faced and had a cast polyamide backing and made of constantan alloy.

A slip ring (Michigan Scientific Model SR10M) was used to transfer strain signals from the rotating shaft to the fixed frame. The strain gauges were all balanced by using 120 O dummy resistors on the spinning side so that a high signal-to-noise ratio is maintained as the signals are transmitted through the slip ring. On the stationary side, the six strain signals were carried to an NI SCXI 1314 terminal block that was connected to an NI SCXI 1520 strain input module. The terminal block and strain input module were housed by an NI SCXI 1000 Chassis. An SCXI 1349 cable assembly connected the chassis, and delivered the data to the computer through a PCI 6052 bus for further processing. The strain signals were analyzed by using LabVIEW and post-processed in MATLAB. The sampling rate was set to 55 kHz in LabVIEW, which was deemed to be sufficient to capture the transients caused by gear tooth impacts allowing 220 data points per mesh period at $\Omega_1 = 300$ rpm for this gear pair. Prior to testing, offset null calibration was performed for all strain gauges internally in NI MAX when gears were unloaded. Strain signals were converted to stresses by applying Hooke's law in a uniaxial manner.

One major challenge with gear root strain measurements is ensuring that gauges of different roots are at the same respective location so that they measure the same strains under quasi-static, constant-torque conditions. Since the stress gradient of the root fillet region is very steep, even a small deviation of the actual position of a gauge in the profile direction from its nominal position can cause the resultant strain signals to change significantly. Fig. 5(a) and (b) show measure stress histories from baseline tests performed at $T_{a1} = T_{a2} = 0$ for $T_m = 10$ and 30 Nm, respectively. Fig. 5(a1,b1) compares the measurements $\sigma_{d,1}$, $\sigma_{d,2}$ and $\sigma_{d,3}$ of the three drive-side gauges, named D1, D2 and D3. Likewise, the signals $\sigma_{c,1}$, $\sigma_{c,2}$ and $\sigma_{c,3}$ shown in Fig. 5(a2,b2) are for the coast-side gauges of C1, C2 and C3, respectively. In each of these figures, three drive-side gauge signals are nearly identical in shape and amplitude and they are spaced one base-pitch from each other. The same observation applies to the coast-side gauges as well, indicating that the gauge placement on the tooth root fillets was done accurately.

Under rattling conditions, impacts can significantly alter the root stress history both quantitatively and qualitatively. The example rattling motion shown in Fig. 3, for instance, spans three complete rotations of the gear pair. Per each rotation, multiple drive-side impacts and a single coast-side impact take place, each impact occurring in a very small rotational increment. Major ones of these impacts are marked on Fig. 3(b). It is clear that only certain teeth of the gear will be in contact (in the meshing zone) when these impacts occur to experience any root stress consequences. Ideally, all of the teeth of the test gear would need to be gauged in order to capture all stresses due to all impacts. This is not feasible as in Fig. 4 where only three successive gauges teeth are instrumented such that it can capture 3/50 the dynamics shown in Fig. 3. It is likely that the gauged teeth would pass through the meshing zone when there are no impact occurring, in the process failing to record the stress consequences of impacts. One practical remedy is to adjust the phase angle ϕ between the body coordinate frame of the instrumented gear and the alternating torque $T_{a1}(t)$ as given in Eq. (3). If the motions are periodic, this phase angle can be adjusted to determine what segment of the $q(t)$ signal is experienced by the gauged segment of the gear when it is at the gear mesh. By performing the same tests at different ϕ, strains caused by motions along different instances of $q(t)$ can be recorded.

Fig. 6 shows the body coordinate frames gears and the positions of the strain gauged teeth. The body coordinate frame (x_i, y_i) is attached to gear i (i.e., rotates with gear i) such that first gauged gear tooth (tooth-1) enters the mesh when $\theta_i(t) = 0$. Depending on the order n_1 of the excitation, spanning $1/n_1$ of a complete rotation of the unity-ratio gears is required to capture any impact related root stresses. This means a span $50/n_1$ teeth. For $n_1 = 3$, for instance, $50/3 = 16.67$ teeth must be spanned in increments of three

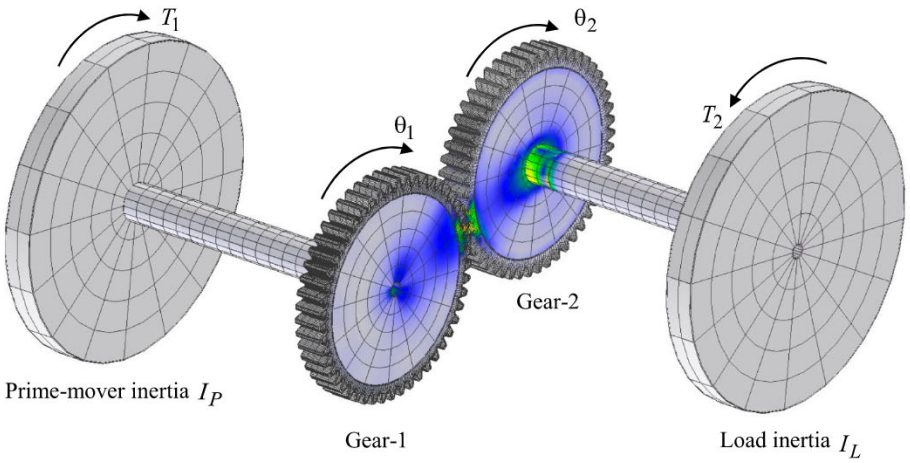

Fig. 7. Deformable-body model of the test gear pairs [33].

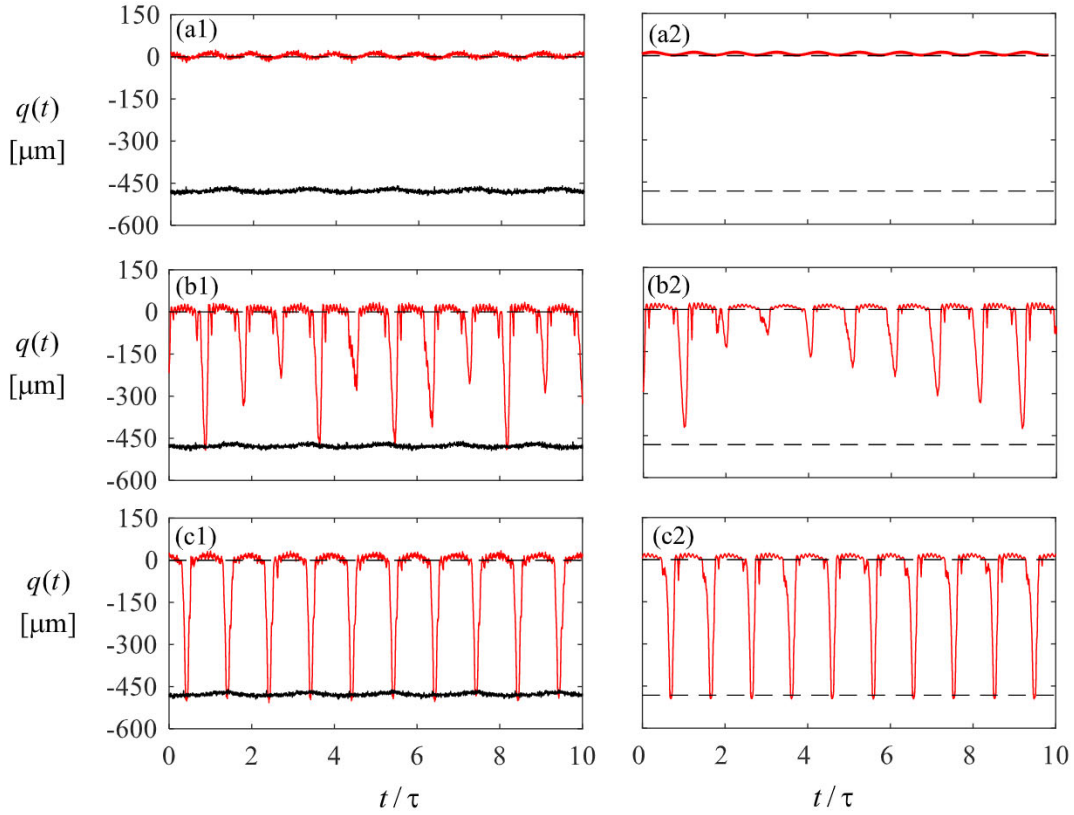

Fig. 8. Representative rattling motions considered in this study obtained by varying T_{a1} at $T_{a2} = 0$, $T_m = 10$ Nm, $\Omega_1 \approx 270$ rpm, and $n_1 = 2$. (a) $T_{a1} = 15.0$ Nm, (b) $T_{a1} = 20.8$ Nm, (c) $T_{a1} = 25.5$ Nm. (a1-c1) are the measurements, and (a2-c2) are the model predictions. Black lines denote backlash boundaries.

instrumented teeth. This can be done by repeating the same test at $16.67/3 \approx 6$ increments of ϕ.

3. Dynamic model

Solution of gear contact problems using conventional finite element tools is not desirable as a very fine finite element mesh is required for the teeth in the contact zone and remeshing is necessary for every rotational increment as the contact lines and the teeth move in time [31,32]. These become even larger issues under dynamic conditions where simulations must be carried out for longer

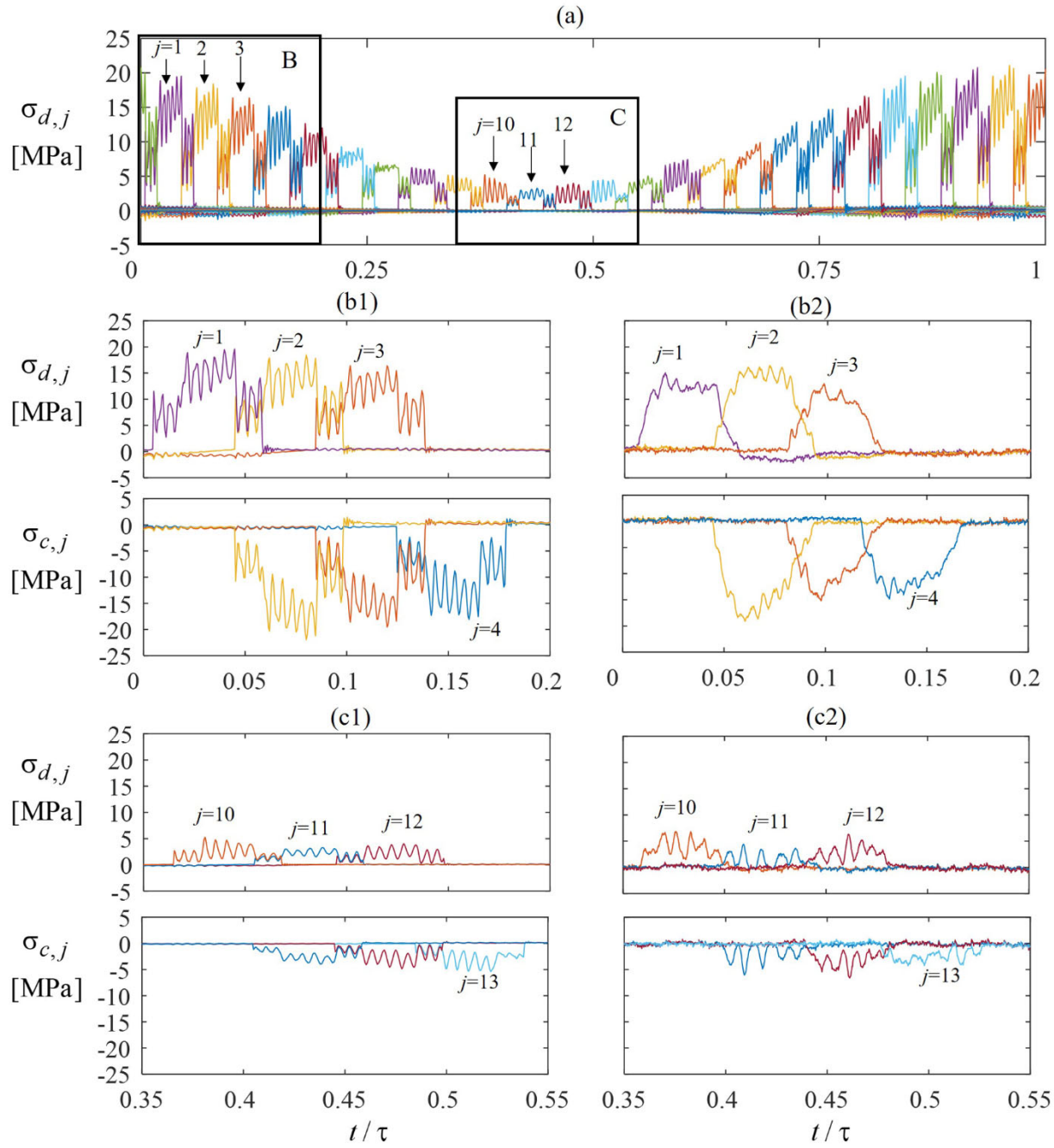

Fig. 9. (a) Predicted drive-side root stresses $\sigma_{d,j}$ at Test-1, (b,c) close-up view of drive and coast-side root stresses in regions denoted by region B and C. (b1,c1) are predictions, and (b2,c2) are measurements.

periods of time at much smaller time increments. In order to overcome such difficulties, a commercial deformable-body contact mechanics tool [33] was used here. This tool employs a semi-analytical formulation based on Bousinesq and Cerruti solutions to model the contact interfaces and conventional finite elements away from the contact interface to account for deformations of gear bodies and the support structures. This approach significantly reduce the model dimension compared to full-scale FE models as it does not require highly refined mesh at the contact zone [34,35]. Under moderately and highly loaded conditions, predictions of this model were shown to correlate well with dynamic transmission error measurements of a single gear pair [23].

This model will be used here to predict root stresses of a unity-ratio spur gear pair of Table 1 under the same operating conditions as experiments at the actual location of the strain gauges. The deformable-body model of the experimental setup of Fig. 1 is shown in Fig. 7. Here prime mover and load inertias $I_L = I_P = 0.033\,\mathrm{kg}\cdot\mathrm{m}^2$ are modeled by disks connected to gears via shafts representing the

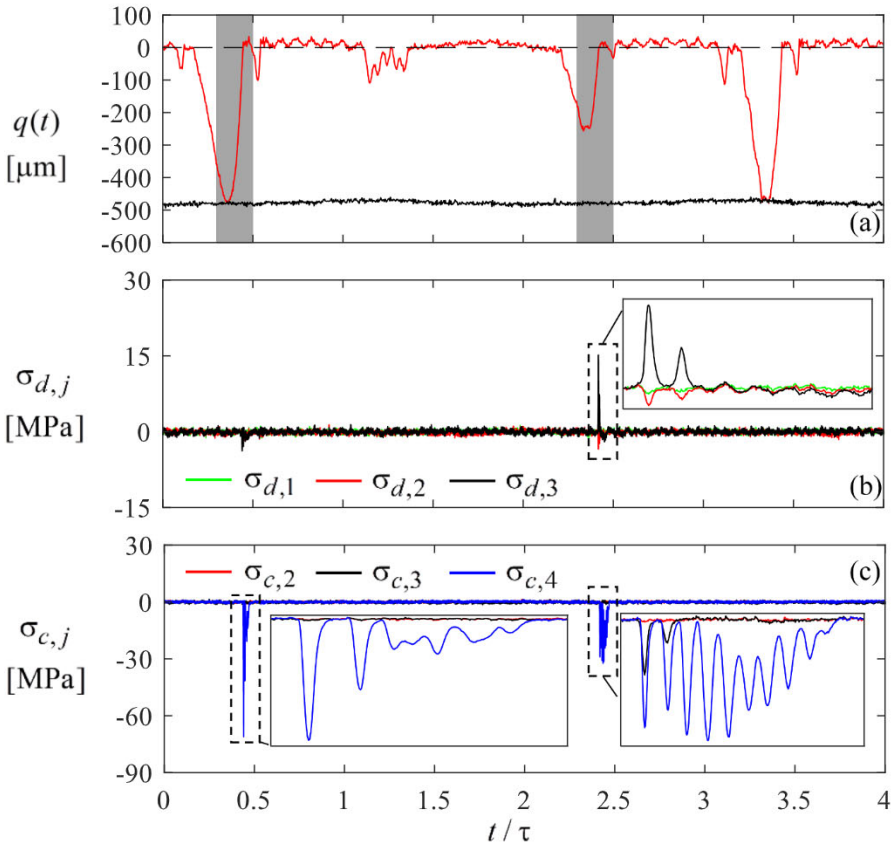

Fig. 10. (a) Measured $q(t)$, (b) drive-side stresses and (c) coast-side stresses of Test-2 at $\phi = 124deg$. The gray boxes in (a) represent the instrumented teeth.

total torsional compliance of the drivetrain $k_t = 16.8\,\text{kNm/rad}$ [18]. The primary energy dissipation mechanism in the deformable-body model is internal damping, defined by a damping matrix $\mathbf{C} = \mu\mathbf{M} + \eta\mathbf{K}$ where $\mathbf{M}$ and $\mathbf{K}$ are the mass and stiffness matrices. Damping parameters of $\mu = 19$ and $\eta = 4.7 \cdot 10^{-6}$ were used in these simulations such that thee modal damping ratio definition of Rayleigh's damping model $\zeta = \mu/2\omega_n + \eta\omega_n/2$ is within $0.01 < \zeta < 0.03$ for the frequency range of interest $80\,\text{Hz} < \frac{1}{2\pi}\omega_n < 1800\,\text{Hz}$. Virtual gauges were placed at all roots of gear 2 along the both drive and coast-side fillets [27]. This allowed prediction of root stresses of every tooth regardless they experience an impact or not. This eliminates the need to run simulations at different phasing ϕ like the experiments. The Newmark scheme was used to numerically integrate the equation of motions with $\gamma = 0.5$ and $\beta = 0.251$ being the Newmark coefficients.

4. Results

Prior characterization of the motions of this system in Section 2.1, namely NI, SSI or DSI, indicated that the last two types of motions allow vibro-impacts. In Ref. [16], these SSI or DSI type rattling motions were further subjected to a classification based on (i) the periodicity of the motion and (ii) number of coast-side impacts per excitation period. With this classification, a rattling $P(m)$ motion denotes a periodic one having m number of coast-side impacts per excitation period.

Fig. 8 shows a set of rattling motions collected using the gear pairs defined in Table 1 under three different excitation conditions. Here, the relative displacement $q(t)$ was measured by varying the amplitude of the alternating torque component T_{a1} between 15.0 and 25.5 Nm for $T_{a2} = 0$, $T_m = 10$ Nm, $\Omega_1 \approx 270$ rpm, and $n_1 = 2$. First, an NI motion is shown in Fig. 8(a) where the contact is maintained all the time along the drive side. This will be called Test-1 condition. Tooth separations occur in Fig. 8(b) for $T_{a1} = 20.8$ Nm. These separations are followed by drive-side impacts while some of them graze the coast-side boundary in Fig. 8(b1). This chaotic motion is considered here as Test-2. Finally, the motion shown in Fig. 8(c) for $T_{a1} = 25.5$ Nm is a periodic one with one coast side impact per excitation period, denoted by $P(1)$, referred to here as Test-3. The deformable-body model is seen to agree with measurements of $q(t)$ for all three cases. These three tests with qualitatively different resultant motions were used to demonstrate how root stresses change under these different *NI*, and periodic and chaotic impact motions. Here, the order $n_1 = 2$ indicates the torque fluctuation frequency is twice the shaft rotation frequency $\frac{2\pi}{60}\Omega_1$ as defined in Eq. (3). In these tests, the mean rotational speed was held within about 10% of

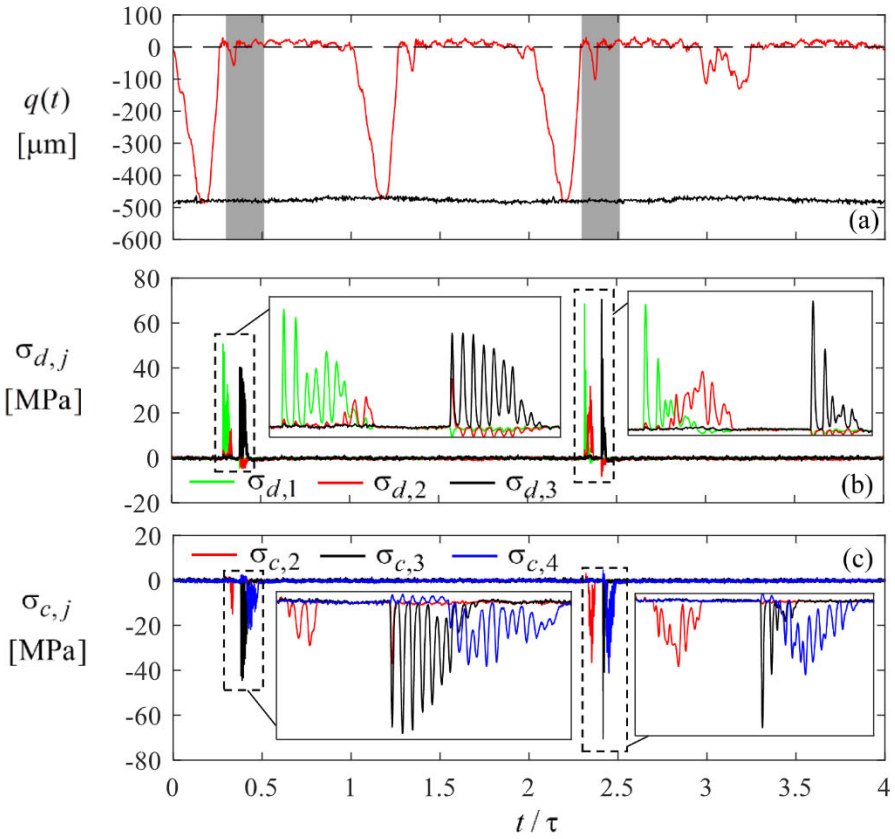

Fig. 11. (a) Measured $q(t)$, (b) drive-side stresses and (c) coast-side stresses of Test-2 at $\phi = 104deg$. The gray boxes in (a) represent the instrumented teeth.

$\Omega_1 = 270$ rpm.

4.1. Root stresses during a baseline No-Impact (NI) motion

As Test-1 of Fig. 8(a), motion is a no-impact (*NI*) motion, it will be treated as a baseline representation of root stresses under no rattling. Fig. 9(a) shows predicted drive-side $\sigma_{d,j}$ time histories for this test during a single selected excitation period τ spanning 25 gear mesh cycles. Here, it is seen that all predicted drive-side stresses $\sigma_{d,j}$ remain positive (tensile) during the entirety of τ for all gear teeth. The instantaneous torque amplitude when tooth j passes through the meshing zone determines the maximum $\sigma_{d,j}$. Stress signals are seen to exceed 15 MPa as the gauged teeth enter the mesh when $T_1(t)$ is at its maximum value of about 25 Nm. Meanwhile the stress amplitudes are lowered to 4 MPa when a gauged tooth is aligned with the minimum value of $T_1(t)$. In between, root stress amplitudes observed in Fig. 9(a) mimics the corresponding $T_1(t)$.

Measured drive and coast-side root stresses that correspond to the regions denoted by B and C on Fig. 9(a) are shown in Fig. 9(b2, c2) with the same axis scales of the corresponding predictions of Fig. (b1,c1). The regions B and C cover the period when gear teeth $j =$ 1–3 and $j =$ 10–12 are in the gear mesh zone, respectively. The phasing methodology described in Section 2.2 was employed in Fig. 9 (b2,c2) to shift the position of the strain gauged teeth with respect to $T_1(t)$, and hence the resultant $q(t)$, allowing one to assess the tooth-to-tooth root stress variation within an entire excitation period τ. The corresponding predictions shown in Fig. 9 (b1,c1) are seen to capture the overall behavior and register similar stress levels except larger fluctuations observed in predicted $\sigma_{d,j}$ and $\sigma_{c,j}$ signals of Fig. 9(b1).

Fig. 9(a) indicates that each tooth is loaded (i.e. its gauges register a non-zero strain) for a period of nearly 0.057 on the t/τ scale. Considering $n_1 = 2$ here ($T_1(t)$ repeats itself twice per rotation of the unity-ratio gear pair) and gears have $N = 50$ teeth each, the gear mesh period is $\tau_m = n_1\tau/N = \tau/25$. This indicates the loaded tooth period cover nearly 1.4 gear mesh cycles, representing the profile contact ratio in line with this gear pair operating at a center distance of 150.5 mm. Another observation that can be made in Fig. 9(b2, c2) is that when the teeth with the strain gauges are not in mesh, they record zero stress with no level difference, implying that the Wheatstone bridge circuit balancing and offset null calibration were effective.

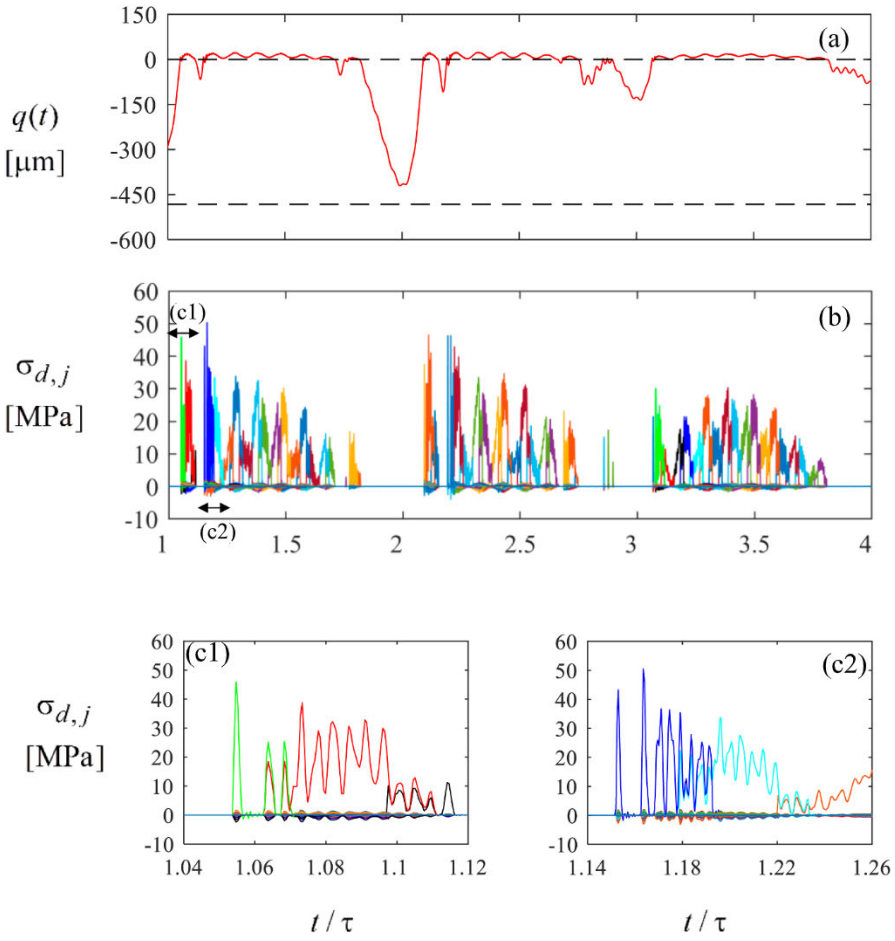

Fig. 12. Predicted (a) $q(t)$ and (b) drive-side root stresses $\sigma_{d,j}$ at the operating conditions of Test-2. (c1-c2) are close-up views of (b).

4.2. Root stresses during a chaotic motion

This section presents the measurement results for the chaotic motion as shown in Fig. 8(b) (Test-2). Since this motion is not periodic, a segment of the $q(t)$ signal that is as long as the period of the excitation is not sufficient to describe the situation. As such, the recorded stress signals at a given ϕ will be presented in two-rotation-long time windows with several consecutive windows considered. For each ϕ, the recorded stress magnitudes are expected to change as impacts in each excitation period are different. As such, the stress time histories must be viewed here cumulatively for longer time periods to form a stress envelope.

Fig. 10 displays 2-revolution-long segments of measurements from Test-2 when $\phi = 124^{\circ}$. Here, the regions when the instrumented teeth are in the gear mesh zone are identified by gray boxes in Fig. 10(a). For each two-revolution segment, four periods of $T_1(t)$ takes place since $n_1 = 2$. As such, while gauged teeth are aligned at this ϕ with positions where drive-side impacts occur, they capture different impact intensities each time. Similar set of measurements at $\phi = 104^{\circ}$ (Fig. 11) are also included here capturing first and secondary drive-side impacts.

Several observations can be made from Figs. 10 and 11 for this chaotic motion. The first drive-side impact had a significant influence on the stress magnitudes, resulting in maximum stresses as high as 71 MPa for $\sigma_{c,4}$ in Fig. 10(c), representing a three-fold increase in comparison to the baseline case. The first and largest stress spike at $t/\tau = 0.48$ was first fully released and then followed by a set of decaying stress spikes as shown in Fig. 10(d). At the next excitation cycle at $t/\tau = 2.4$, the amplitude of the subsequent dynamic spikes reaches the first spike amplitude, suggesting that they might not be negligible in terms of their fatigue consequences. The second drive-side impact while looking harmless on $q(t)$ signal resulted in large root stress values due to its high impact velocity [18]. While these second drive-side impacts consistently corresponded to a tooth separation of 50 μm or less, they resulted in stress spikes of nearly 70 MPa (displayed by $\sigma_{c,3}$ in Fig. 11(c) at $t/\tau \approx 2.4$), nearly three times larger than the baseline measurement with no impact. Shapes of the root stresses caused by the second drive-side impacts comprised of two main shapes. One type is similar to that of the first drive-side impact where a large amplitude spike followed by subsequent smaller spikes. A good example of this is seen in $\sigma_{d,2}$ and $\sigma_{c,2}$ in Fig. 11(b,c) at $t/\tau \approx 2.45$. The other type contains multiple subsequent dynamic stress spikes with amplitudes equal to or

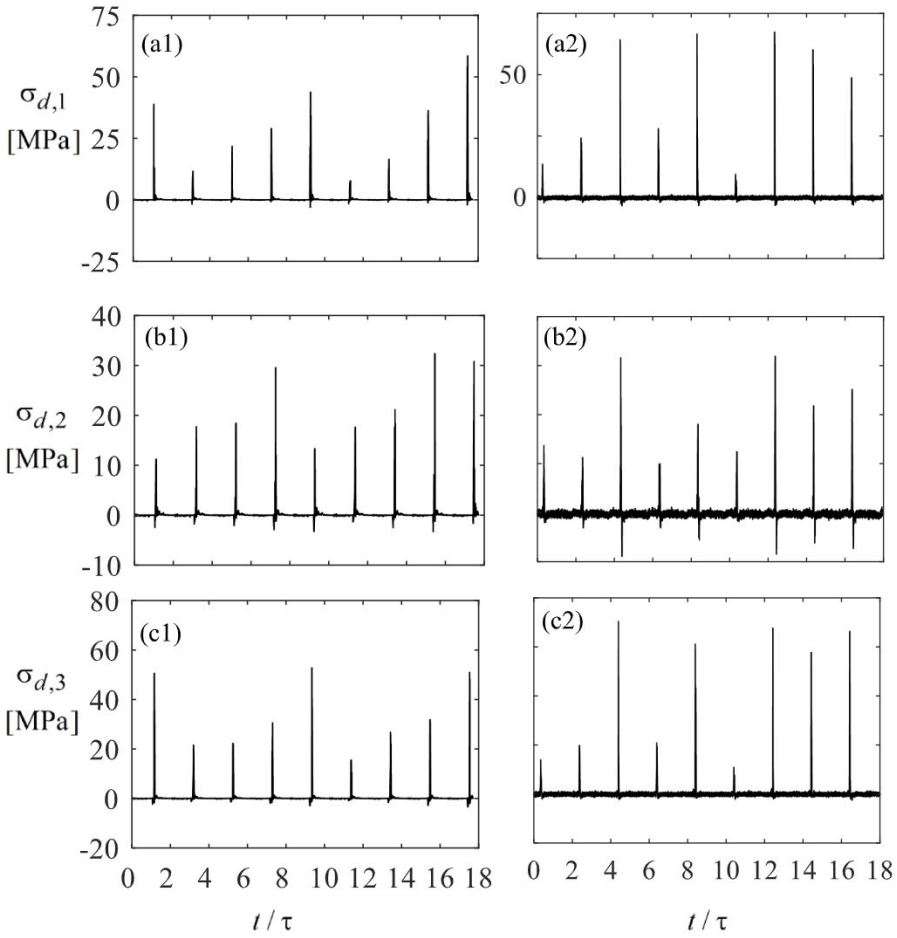

Fig. 13. (a1-c1) Predicted and (a2-c2) measured drive-side root stress time histories over 18 forcing cycles for Test-2 at $\phi = 104\,deg.$

larger in size than the first spike amplitudes (i.e. $\sigma_{c,3}$ in Fig. 11(c) near $t/\tau = 0.45$), where the loading is fully released between each successive amplitude.

Predicted drive-side root stresses $\sigma_{d,j}(t)$ for all gear-2 teeth $j \subset [1, 50]$ are displayed in Fig. 12(b) for 3 excitation periods period τ, corresponding to the predicted $q(t)$ shown in Fig. 12(a). All $\sigma_{d,j}(t)$ signals register zero stress during the separations followed by drive-side impacts with increased root stress levels. Zoomed views of those impact zones shown in Fig. 12(c1-c2) indicate fully-released stress peaks that decay in amplitude agreeing with measurements of Fig. 10 qualitatively. As $q(t)$ is not periodic, each tooth encounters different intensities of impact making impossible to make a quantitative comparison between predictions and measurements.

Depending on the relative phase with respect to the excitation period τ and where the impacts occur within this period, a single tooth undergoing chaotic impacts experiences a wide range of stress amplitudes. 12-revolution-long measured stress time histories are presented in Fig. 13 for an example phasing value of $\phi = 104^{\circ}$ along with the corresponding predictions. Mostly the highest spike of each impact induced stress event is obvious in these figures as the time scale has been compressed to fit 12 gear revolutions. These highest stress peaks are seen to vary significantly for each excitation period. A good agreement is observed between the predictions and measurements in terms of ranges of the peak amplitudes. Following each of these highest spikes, there are multiple fully-released post-spikes having comparable amplitudes. For instance, gauge $\sigma_{d,3}$ of tooth-3 in Fig. 11(b) near $t/\tau = 0.5$ registers a first spike amplitude of 40.3 MPa, followed by other fully-released spikes at amplitudes of 40.3, 39.8, 35.1, and 33.7 MPa. This indicates that each impact event has the potential of causing up to 5 to 7 individual stress spikes that might influence the fatigue life of the tooth adversely. Over the course of 12 gear rotations, the same tooth-3 is seen to experience stress amplitudes ranging from 10.3 to 70.4 MPa (Fig. 13(c2)), or 0.5 to 3.5 times the maximum NI stress levels in Section 4.1.

4.3. Root stresses during a P(1) motion

Root stresses occurring during the periodic $P(1)$ motion of Fig. 8(c) (Test-3) are presented next in Fig. 14. For $P(1)$ motion shown in Fig. 14(a), two impacts are of main interest here, one coast-side impact when crossing from Regime II to Regime III (box B), and then

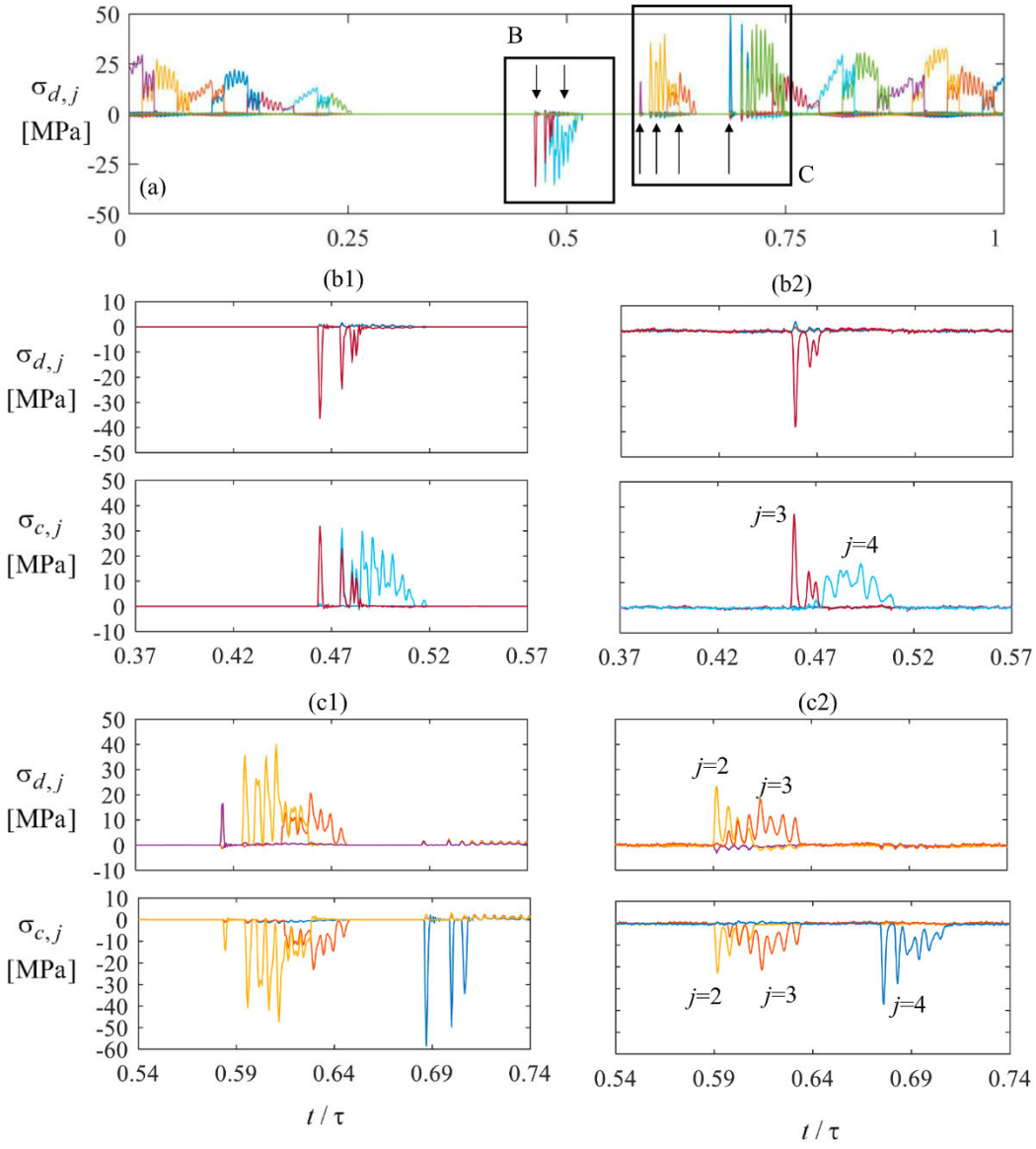

Fig. 14. (a) Predicted drive-side root stresses $\sigma_{d,j}$ at Test-3, (b,c) close-up view of drive and coast-side root stresses in regions denoted by region B and C. (b1,c1) are predictions (b2,c2) are measurements.

the drive-side impacts when crossing from Regime II to Regime I (box C). When $t/\tau < 0.25$, the instrumented teeth go through the gear mesh when the drive-side contact is maintained. As such, $\sigma_{d,j}$ resembles the NI Test-1 results. When $0.25 < t/\tau < 0.46$, gauged teeth pass through the mesh zone without any contact since the gear pair is in Regime II during their entire travel through the gear mesh zone. As such, all $\sigma_{d,j}$ record zero stresses. Meanwhile, a large compressive stress spike of 38 MPa is observed in $\sigma_{d,j}$ signal of Fig. 14(b1) agreeing with the corresponding measurement shown in Fig. 14(b2). In the same figures, coast-sides of gauged teeth $\sigma_{c,j}$ exhibit a positive spike of the same magnitude. It is also observed that tooth-4 is in gear mesh when the contact is maintained in the coast side after the coast-side impact, so that $\sigma_{c,4}$ shows a tensile stress with no impact consequences. In Fig. 14(c2), tooth-2 and tooth-3 experience the first drive-side impact followed by a small separation from the drive-side boundary and the second drive-side impact as evidenced by zero stress recording in between at $t/\tau \subset [0.64, 0.67]$ and large amplitude $\sigma_{c,4}$ fluctuations starting at $t/\tau = 0.67$. It is also worth noting that the second drive-side impact shown in Fig. 14(c2) also indicates that the spike of $\sigma_{c,4}$ reaching 37 MPa is fully released, followed by smaller spikes of decaying amplitudes. It should be also noted that the maximum stress levels for this $P(1)$ motion are below the corresponding maximum value of 71 MPa for the chaotic motion of Section 4.2. When $t/\tau > 0.75$, the instrumented teeth enter the gear mesh while drive-side contact is maintained showing no impact induced consequences.

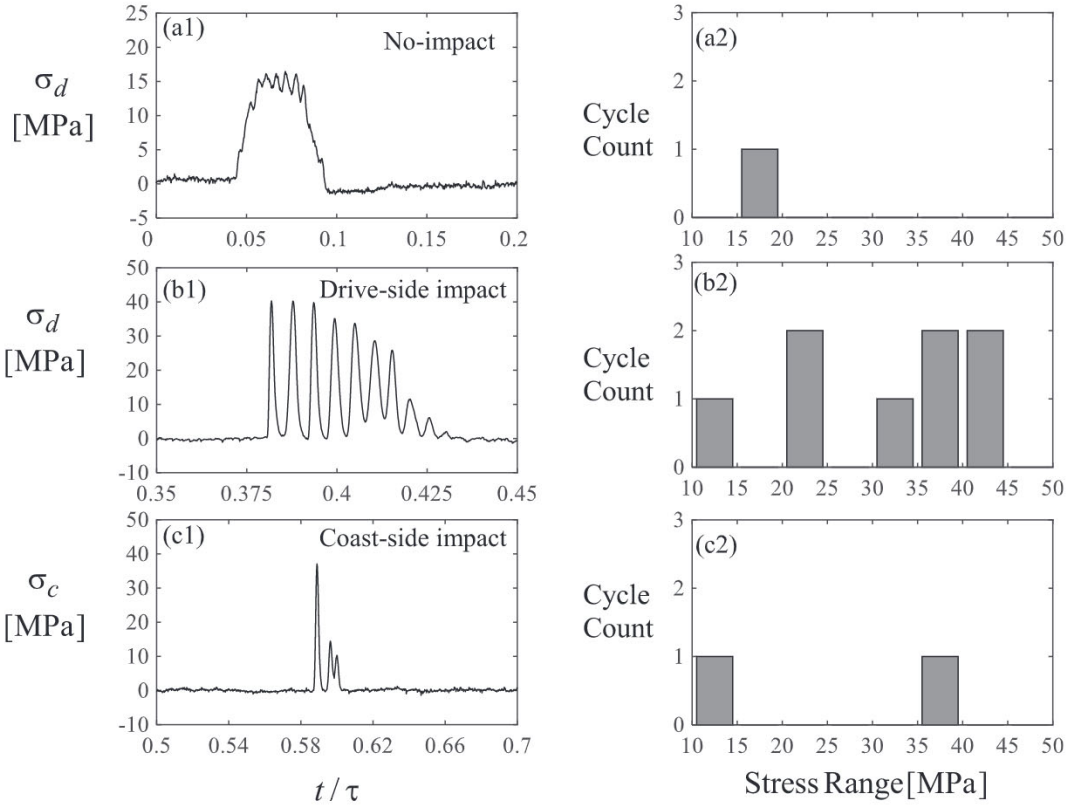

Fig. 15. (a1-c1) Example measured root stress histories from Fig. 9(b2), 11(b), and 14(b2), respectively, and (a2-c2) corresponding stress amplitude versus cycle counts obtained by rainflow analysis.

5. Discussion

Figs. 10–14 showed that gear rattling has two major effects on the stress histories. First, impacts during gear rattle conditions increase the maximum root stress amplitudes several times compared to a corresponding no-rattle situation such as Fig. 9. Secondly, such stress spikes are followed by several additional fully-released spikes with amplitudes that are comparable in size to that of the first spike. Significant increases in amplitudes and frequency of these stress spikes caused by rattling impacts can be expected to affect the fatigue performance of the gear pair adversely. In order to demonstrate this, three example tooth stress $\sigma(t)$ signals, one from each of the NI, chaotic, and $P(1)$ motions of the previous section, are considered in Fig. 15(a1-c1). Rainflow Cycle Count Method [36] is used to define corresponding fatigue loading cycles that must be considered in a cumulative damage calculation. Fig. 15(a2-c2) shows the cycle counts along with corresponding stress ranges associated with these three tooth loading events. Cycles with amplitudes lower than 10 MPa are not considered here as they might not be significant in terms of fatigue damage. While the rainflow analysis counts a single cycle at stress range of 15–20 MPa for no-impact case of Fig. 15(a1), five fatigue loading cycles are counted for the impact event of the chaotic motion within stress range of 30–45 MPa and 3 cycles in the 10–25 MPa range. Meanwhile, the coast-side impact of the $P(1)$ motion is found to represent 1 loading cycle within the stress range of 10–15 MPa and another one within 35–40 MPa. This illustrates how impacts might increase the cumulative damage to gear teeth to affect life span of the gear. The same methodology can be applied to longer durations of stress signals to capture both tensile and compressive stress spikes representative of true duty cycle of a gear tooth. It can also highlight the fact that certain teeth that are consistently in the gear mesh zone when impacts occur will have significantly less life than other teeth avoiding impacts, making them the failure spots.

6. Conclusion

An experimental investigation of the effect of gear rattle on root stresses of a high-accuracy spur gear pair was performed in this study. A previously developed test machine [18] designed to simulate gear rattle conditions was equipped with strain gauge data acquisition and measurement systems to measure strains from a unity-ratio spur gear pair. A methodology was introduced to vary the phasing of the user generated alternating torque component with respect to the position of the strain gauged teeth to capture the gear rattle impacts. The phasing methodology was shown to simulate tooth root stresses during a single excitation frequency for periodic motion types at different gear mesh positions. It also exhibited tooth root stresses for gauged teeth in the gear mesh zones for chaotic motion types occurring at different intensities. Drive-side impacts during gear rattle conditions consistently registered greater

maximum root stresses than coast-side impacts and resulted in stress values up to four times higher than the baseline test when no tooth separation occurred. Drive-side impacts during non-periodic motion were typically two times higher than periodic motion. Root stress results from coast-side impacts were considerable, and increased in magnitude with increasing alternating torque, reaching maximum values that are several times greater than the no-impact experiments. Furthermore, impacts were shown to cause increased number of loading cycles with increased cumulative damage to gear teeth. Developed deformable-body model was shown to be accurate in predicting the behavior of root stresses under impacting conditions.

Declaration of Competing Interest

The authors declare that they have no known competing financial interests or personal relationships that could have appeared to influence the work reported in this paper.

Data availability

The authors confirm that the data supporting the findings of this study are available within the article.

Acknowledgement

Authors thank Dr. S. Vijayakar of Advanced Numerical Solutions, Inc. for providing Transmission3D software for the deformable-body model used in this study.

References

[1] K. Karagiannis, F. Pfeiffer, Theoretical and Experimental Investigations of Gear-Rattling, Nonlinear Dyn. 2 (1991) 367–378.
[2] R. Singh, H. Xie, R.J. Comparin, Analysis of Automotive Neutral Gear Rattle, J. Sound Vib. 131 (1989) 177–196.
[3] A. Baumann, B. Bertsche, Experimental Study on Transmission Rattle Noise Behaviour with Particular Regard to Lubricating Oil, J. Sound Vib. 341 (2015) 195–205.
[4] Y. Kadmiri, E. Rigaud, J. Perret-Liaudet, L. Vary, Experimental and Numerical Analysis of Automotive Gearbox Rattle Noise, J. Sound Vib. 331 (13) (2012) 3144–3157.
[5] C. Padmanabhan, T.E. Rook, R. Singh, Modeling of Automotive Gear Rattle Phenomenon: State of the art, SAE Technical Paper 951316 (1995).
[6] E. Slavkovsky, M. Inalpolat, A. Flodin, An analytical investigation of rattle characteristics of powder metal gears, in: ASME 2019 IDETC International Conference, Anaheim, CA, USA, 2019.
[7] A. Fernandez-Del-Rincon, A. Diez-Ibarbia, S. Theodossiades, Gear Transmission Rattle: Assessment of Meshing Forces under Hydrodynamic Lubrication, Appl. Acoust. 144 (2019) 85–95.
[8] H.H. Miyasato, V.G.S. Simionatto, M.D. Junior, Study of the gear rattle phenomena in automotive powertrain systems, in: 21st International Congress of Mechanical Engineering, Natal, Brazil, 2011.
[9] F. Pfeiffer, W. Prestl, Hammering in Diesel-Engine Driveline Systems, Nonlinear Dyn. 5 (4) (1994) 477–492.
[10] J.C. Huang, K.R. Abram, Cummins 4B Noise Reduction Anti-Backlash Camshaft Gear, SAE Technical Paper 1999-01-1761, 1999.
[11] H.A. Zhao, T.E. Reinhart, The Influence of Diesel Engine Architecture on Noise Levels, SAE Technical Paper 1999-01-1747, 1999.
[12] B. Sobecki, P. Davies, J.S.S. Bolton, F. Eberhardt, Perception of Diesel Engine Gear Rattle Noise, SAE Int. J. Passenger Cars Mech. Syst. 8 (3) (2015) 1097–1103.
[13] G.V. Glyniadakis, A.B. de Souza, M.M. Pecula, M.C. Rodrigues, J.M. Dos Santos, 2010, Diesel Engine Air Compressor Rattle Noise, SAE Technical Paper 2010-01-1540.
[14] M.D. Croker, S.a. Amphlett, A.I. Barnard, Heavy Duty Diesel Engine Gear Train Modelling to Reduce Radiated Noise, SAE Technical Paper 951315 (1995).
[15] P. Ziegler, P. Eberhard, Simulative and Experimental Investigation of Impacts on Gear Wheels, Comput. Methods Appl. Mech. Eng. 197 (51–52) (2008) 4653–4662.
[16] A. Donmez, A. Kahraman, Characterization of Nonlinear Rattling Behavior of a Gear Pair Through a Validated Torsional Model, J. Comput. Nonlinear Dyn. 17 (4) (2022), 041006.
[17] A. Donmez, A. Kahraman, Vibro-Impact Motions of a Three-Degree-of-Freedom Geartrain Subjected to Torque Fluctuations: Model and Experiments, J. Comput. Nonlinear Dyn. 145 (1) (2023), 011007.
[18] A. Donmez, A. Kahraman, Experimental and Theoretical Investigation of Vibro-Impact Motions of a Gear Pair Subjected to Torque Fluctuations to Define a Rattle Noise Severity Index, J. Vib. Acoust. 144 (4) (2022), 041001.
[19] A. Donmez, A. Kahraman, A Rattle Noise Severity Index for Multi-mesh Gear Trains Subjected to Torque Fluctuations, J. Vib. Acoust. 145 (1) (2022), 011007.
[20] A. Donmez, A. Kahraman, An Experimental and Theoretical Investigation of the Influence of Backlash on Gear Train Vibro-impacts and Rattle Noise, Proc. Inst. Mech. Eng. Part K.
[21] A. Donmez, A. Kahraman, Influence of Various Manufacturing Errors on Gear Rattle, Mech. Mach. Theory 173 (2022), 104868.
[22] G.W. Blankenship, A. Kahraman, Steady State Forced Response of a Mechanical Oscillator with Combined Parametric Excitation and Clearance Type Non-linearity, J. Sound Vib. 185 (5) (1995) 743–765.
[23] V.K. Tamminana, A. Kahraman, S. Vijayakar, A Study of the Relationship Between the Dynamic Factors and the Dynamic Transmission Error of Spur Gear Pairs, J. Mech. Des. 129 (1) (2006) 75.
[24] A. Kahraman, G.W. Blankenship, Experiments on Nonlinear Dynamic Behavior of an Oscillator With Clearance and Periodically Time-Varying Parameters, J. Appl. Mech. 64 (1997) 217–226.
[25] M.J. Handschuh, A. Kahraman, M.R. Milliren, Impact of tooth spacing errors on the root stresses of spur gear pairs, J. Mech. Design Trans. ASME 136 (6) (2014) 1–10.
[26] M. Inalpolat, M. Handschuh, A. Kahraman, Influence of Indexing Errors on Dynamic Response of Spur Gear Pairs, Mech. Syst. Sig. Process. 60–61 (2015) 391–405.
[27] M.A. Hotait, A. Kahraman, Experiments on the Relationship between the Dynamic Transmission Error and the Dynamic Stress Factor of Spur Gear Pairs, Mech. Mach. Theory 70 (2013) 116–128.
[28] D. Talbot, A. Sun, A. Kahraman, Impact of Tooth Indexing Errors on Dynamic Factors of Spur Gears: Experiments and Model Simulations, J. Mech. Design Trans. ASME 138 (9) (2016) 1–13.
[29] I.J. Hong, A. Kahraman, N. Anderson, A rotating gear test methodology for evaluation of high-cycle tooth bending fatigue lives under fully reversed and fully released loading conditions, Int. J. Fatigue 133 (2020), 105432.
[30] M.R. Kang, A. Kahraman, An experimental and theoretical study of the dynamic behavior of double-helical gear sets, J. Sound Vib. 350 (2015) 11–29.

[31] S. Vijayakar, H. Busby, L. Wilcox, Finite element analysis of three-dimensional conformal contact with friction, Comput. Struct. 33 (1) (1989) 49–61.
[32] C. Yuksel, A. Kahraman, Dynamic Tooth Loads of Planetary Gear Sets Having Tooth Profile Wear, Mech. Mach. Theory 39 (7) (2004) 695–715.
[33] Transmission3D, Advanced Numerical Solutions Inc 2019 Hilliard, OH.
[34] S.M. Vijayakar, H.R. Busby, D.R. Houser, Linearization of Multibody Frictional Contact Problems, Comput. Struct. 29 (4) (1988) 576.
[35] R.G. Parker, S. Vijayakar, T. Imajo, Non-Linear Dynamic Response of a Spur Gear Pair: Modelling and Experimental Comparisons, J. Sound Vib. 237 (3) (2000) 435–455.
[36] J.A. Collins, Failure of materials in mechanical design: analysis, prediction, prevention, John Wiley, New York, 1993.